WELDING RESEARCH

SUPPLEMENT TO THE *WELDING JOURNAL*, 2024
Sponsored by the American Welding Society

An Analytical Model of Material Deformation During Friction Welding of Alloy 718

Model for rotary friction welding exhibits higher strain rate in material flow

BY C. BROWN, T. W. NELSON, AND C. D. SORENSON

Abstract

A new model of the material flow in rotary friction welding of tubes is proposed. The material flow proposed is based on 3D microcomputer tomography scans of welds performed with tungsten tracers. The tracers indicate a bifurcation of flow into two deformation paths. The material in Path 1 interacts with the weld interface and exhibits large azimuthal flow. The material in Path 2 transitions from axial to primarily radial flow with little or no azimuthal flow. The directional transition in this path is compared to orthogonal machining and equal channel angular pressing. The process to estimate the variables needed to calculate strain and strain rates using the equations from orthogonal machining and equal channel angular pressing is defined. Strain and strain rate in Path 2 are dependent upon feed rate and upset and decrease throughout the welding process. The strain rate is higher than previously reported for rotary friction welding as a result of the deformation model proposed.

Keywords

- Rotary Friction Welding
- Material Flow
- Strain Rate
- Model
- Alloy 718

Introduction

Rotary friction welding (RFW) is a solid-state joining process in which heat is generated by the relative motion at the interface between the work pieces. The material flow is essential in removing contaminants from the weld interface (Ref. 1).

There are two types of RFW: inertia friction welding (IFW) and direct drive friction welding (DDFW). In IFW, the rotating piece is attached to a flywheel, whereas in DDFW, the rotating piece is spun by a motor. In DDFW, the process is in a quasi-steady state between the initial torque peak and the braking/forging phase. The current paper investigates the material flow during the quasi-steady state stage. The material flow during the quasi-steady state stage in both IFW and DDFW are similar (Ref. 1).

A cylindrical coordinate system, shown in Fig. 1, describes the direction of material flow. Any flow in the direction is assumed to be axisymmetric and is called azimuthal flow in the present study.

Many contemporary methods to model material flow during the quasi-steady state stage are finite element analysis (FEA) based. Grant et al. (Ref. 2) used FEA with no azimuthal flow to calculate strain rates as high as 4 in. nickel-based superalloy RR1000. Using a full 3D rigid viscoplastic FEA model, Zhang et al. (Ref. 3) calculated strain rates as high as 0.77 in. nickel-based superalloy GH4169. Due to the limitations of remeshing and element size, FEA-based methods cannot capture the high strain rates present at the weld interface (Ref. 2).

Analytical models have been created to model the material flow and temperature profile in friction welding. Li et al. (Ref. 4) created an analytical model of the weld interface during the 1st stage of an RFW using the assumption that the material acts as a non-Newtonian fluid. The strain rates for these methods vary depending on sample geometry and material but usually are between 102 and 104.

FEA and analytical models capture the material flow at different locations within the deformation region, resulting in a large difference in the strain rates reported from the two methods. To capture both deformation characteristics, Midling (Ref. 5) proposed a stepwise 3D velocity field with two regions. These two regions were defined as the fully plasticized region and the partly deformed region.

https://doi.org/10.29391/2024.103.014

The two regions differ in their azimuthal flow characteristics. In the fully plasticized region (Z < 0.5 in the example from the paper shown in Fig. 2), there is an azimuthal velocity of large magnitude. The fully plasticized region has a strain rate reported between 102.5 and 104 (Ref. 5). The material in the partly deformed region is assumed to have no azimuthal flow. The strain rate in the partly deformed region is reported to be 100. In this model, there is a gradual transition from axial velocity to radial velocity.

When comparing the results from Midling (Ref. 5) to microstructure analyses, there are discrepancies in how the material flows in the RZ plane. In the microstructure analyses in Fig. 3, the transition from axial to radial happens abruptly (transition indicated by the red lines) (Ref. 6). The material recrystallizes at the entry of the HAZ (blue line), but the flow direction remains axial until the red line.

Although useful for the validation of velocity fields in the RZ plane, microstructure analyses like those shown in Fig. 3 cannot quantify or validate azimuthal flow. The current paper uses a 3D method to quantify azimuthal flow throughout the entire deformation region. Using the 3D results, the current paper proposes a new analytical model for the material flow.

Methods

The experimental study uses thin-walled samples that have an inside and outside radius of 10.16 and 12.70 mm, respectively. The material is nickel-based superalloy 718. The present study uses DDFW performed at 1000 RPM. The feed rates used in the welds are either 1, 2, or 4 mm/sec. Weld samples extended 25 mm beyond the tool holder.

Metallography was performed using Kalling's No. 2 to investigate the thickness of the weld interface.

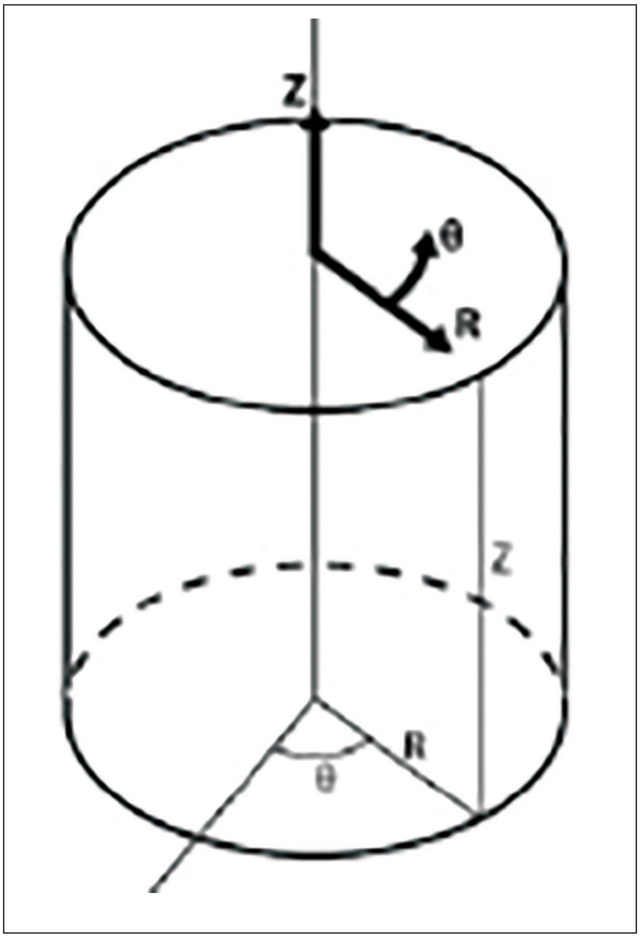

Fig. 1 — Cylindrical coordinates used in the present study.

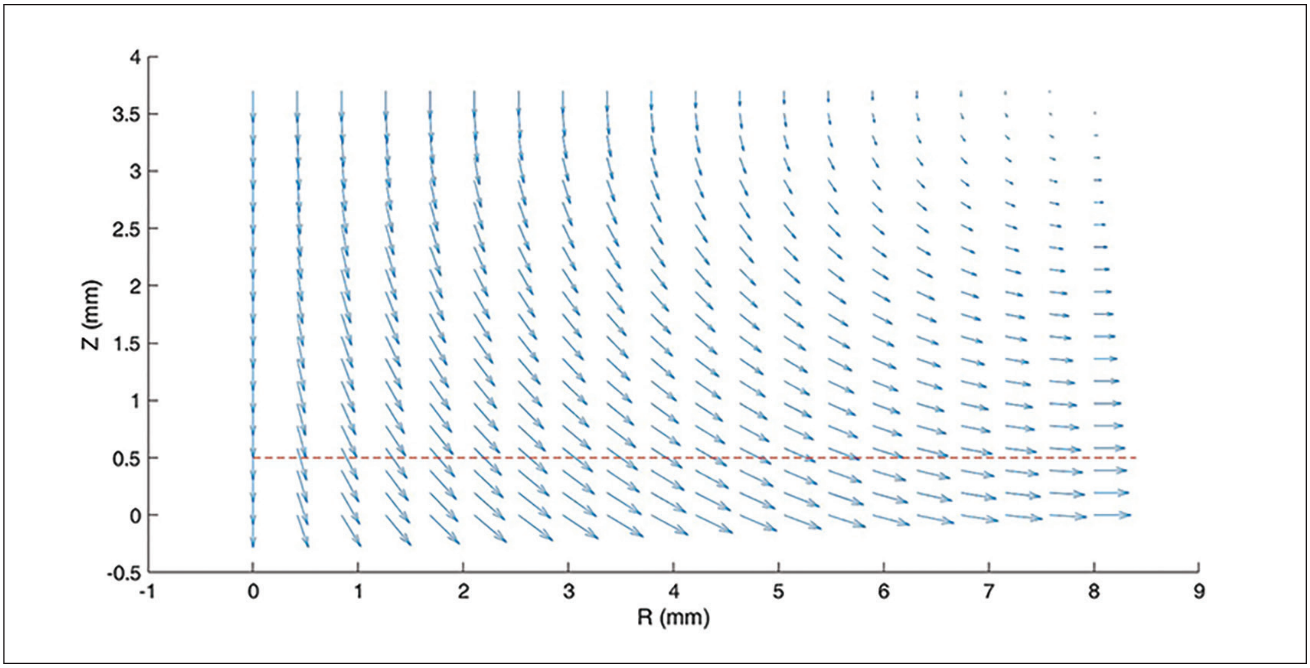

Fig. 2 — Velocity field as a function of axial (Z) and radial (R) distance in the RZ plane as proposed by Midling (Ref. 5).

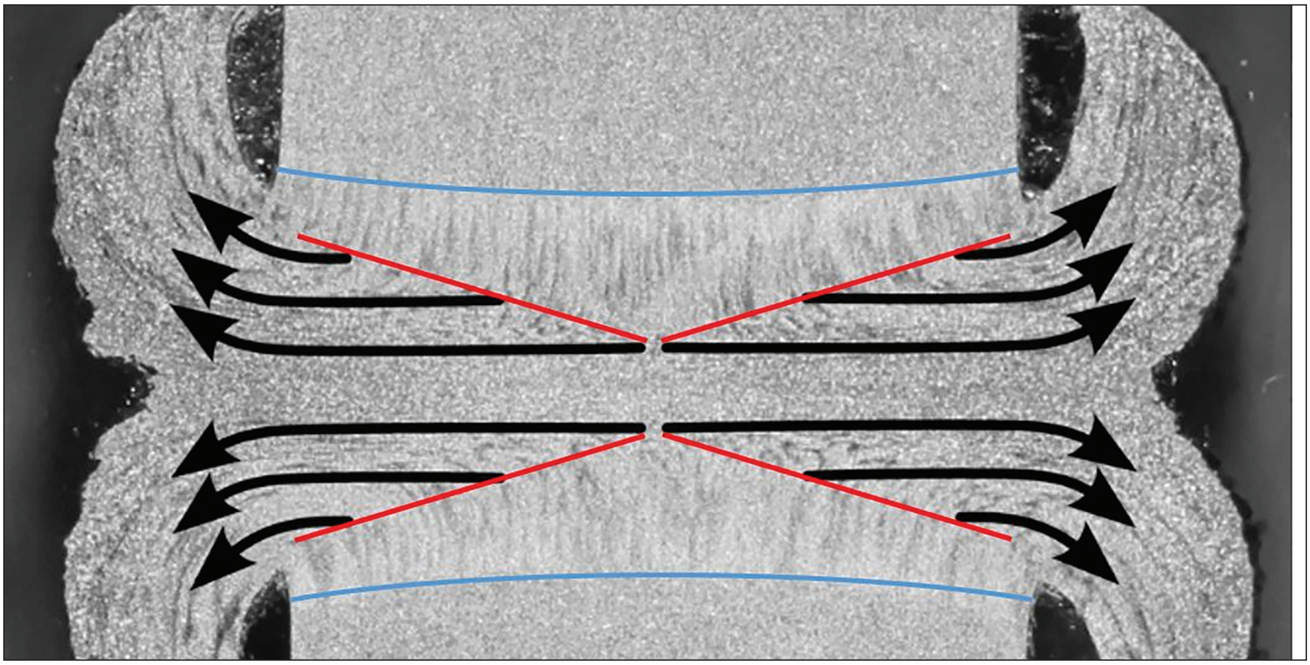

Fig. 3 — Material flow in RFW of steel (Ref. 6).

To investigate the material flow, tracers were placed in various locations throughout the wall thickness. Microcomputer tomography (µCT) was used to get 3D scans of the welded samples. Tungsten was chosen as the tracer material so that the density of the tracer and sample could be distinguished in the scan. Welds were run with either tungsten wire or tungsten powder as the tracer material. The bulk hot strength of the wire is higher than superalloy 718, which necessitates the use of the powdered form as an opposing bound of the material flow.

The tungsten wire has a diameter of 0.229 mm. The powder has an average particle size of 7 microns. Both were inserted into axial holes 0.254 mm in diameter and 2 cm in depth created by a plunge electrical discharge machining. The location of the center of the hole was measured and the location was non-dimensionalized using the following equation:

$$P = (r_t racer - 0.5 * ID)/\big(0.5 * (OD - ID)\big) - 0.5 \qquad (1)$$

This equation is defined such that the ID, center of the wall thickness, and OD are −0.5, 0, and 0.5, respectively.

To quantify the material flow in the azimuthal direction, the angle φ is measured by the method shown in Fig. 4A. The green line is drawn through the centers of the undeformed tracer and the tracer in the flash, as shown in Fig. 4A. Figures 4A–C show the same tracer in the Rθ plane at Z values of 1.4, 0.8, and 0.5 mm, respectively, as shown in Fig. 5. The tracer for all Z values lies on the green measurement line for the angle φ, therefore the value of φ is assumed constant throughout the entire weld process.

To quantify the transition from axial to radial material flow, a circle was fit to the tracer within the deformation zone, as shown in Fig. 5. Each powder tracer exhibited two different radii, with a smaller one closer to the center of the wall thickness, as shown in Fig. 6. Wire tracers were fitted with a single radius.

Results and Discussion

Tracer Analysis

The azimuthal displacement of the tracers (φ) is plotted as a function of position in Fig. 7. The data indicates that the amount of azimuthal flow has a strong dependence on position. Material flow close to the center of the wall thickness, $-0.1 < P < 0.1$, is primarily azimuthal, $\varphi > 75$ deg, while material outside of this region exhibits limited azimuthal flow material flow, $\varphi < 38$ deg. The tracer that does not follow the trend is the result of the wire interacting with both types of material flow simultaneously.

Figure 8 shows the linear dependency of the azimuthal flow of tracers outside the central region ($P < -0.1$ and $P > 0.1$) on feed rate (F) over the range of feed rates used in the current study. The increase in φ with feed rate is expected given that faster feed rates have higher magnitudes of torque, which would promote larger azimuthal deformation.

The tracer study also provides insight into the material flow in the deformation zone through the measurement of the tracer radii. The tracer radii throughout the wall thickness can be used to evaluate the relationship between position and radii proposed by Midling et al. (Ref. 5) in Fig. 2. In the model, the material at the center ($R = 0$) exhibits a large deformation radius, and the material at the edge of the sample exhibits an infinitesimally small deformation radius, as indicated by the dashed line in Fig. 9.

The absolute value of P is used as the position variable to enable a comparison between the tubular specimens in the current investigation and the solid samples in the study by Midling (Ref. 5). Both position variables are always positive

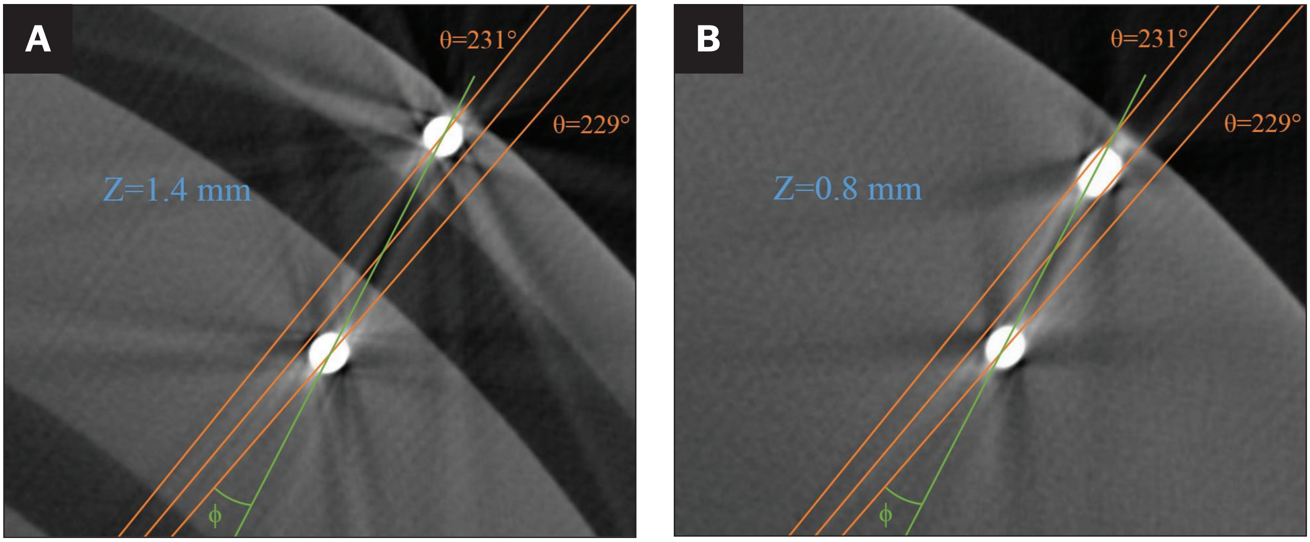

and measure the distance from the point of symmetry (R = 0 in solid and P = 0 in tube).

An example of the relationship between position and radius as proposed by Midling (Ref. 5), as well as the tracer radii from the present study are plotted in Fig. 9. There are several subsets of data in Fig. 9 from the tracer study in the present work. These subsets result from different feed rates, tracer material, and powder exhibiting two different radii as shown in Fig. 6. The small number of data points in each subset as well as the small range of the position variable both make the analysis of a relationship between position and tracer radii difficult.

A simple analysis of Fig. 9 cannot completely prove or disprove the model proposed by Midling (Ref. 5). Therefore, a statistical analysis was performed on the data of the present study.

To investigate the statistical significance of the position of the tracer on tracer radii, the following equation was fit to the data:

$$R = C * abs(P)/F^{D} \tag{2}$$

where C and D are values that are calculated in the fit. This model was chosen because the distribution of the error is normal. To be analyzed as a linear equation, a log transform was performed on both sides, resulting in:

$$\log(R) = \log(C) + \log(abs(P)) - D * \log(F) \tag{3}$$

The values of C and D are group dependent. The grouping variable allows the model to differentiate between wire radii, powder small radii, and powder large radii. This model was

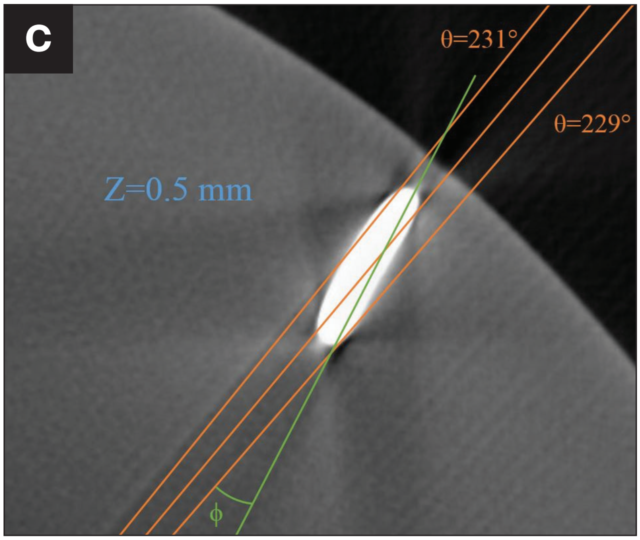

Fig. 4 — Micro CT images of tracer in the Rθ plane and measurement of φ at three Z positions: A — 1.4 mm; B — 0.8 mm; C — 0.5 mm.

chosen because the addition of more variables would increase the complexity of the model without increasing the R2 value. The removal of any term except for log(abs(P)) results in a significant decrease in the R2 value.

The only statistically significant variables are feed rate and the tracer type. The position variable abs(P) has a p-value of 0.5526, indicating that the dependency of radius on the position as proposed by Midling et al. (Ref. 5) is statistically insignificant. Therefore, the present analysis disproves the velocity profile in the RZ plane defined by Midling et al. (Ref. 5) as a model for material flow in RFW of thin wall tubes.

Proposed Material Flow Model

The zones and deformation paths in the following proposed model of the material flow were based on the results of the 3D tracer analysis. The model must include a bifurcation of

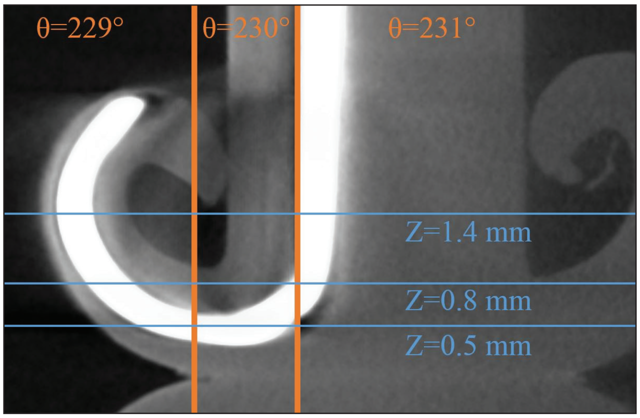

Fig. 5 — Micro CT image of tracer in the RZ plane.

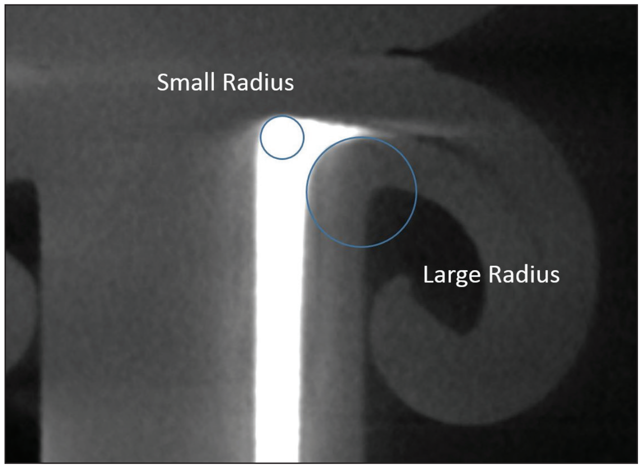

Fig. 6 — Measurement of tungsten powder radii from micro CT results.

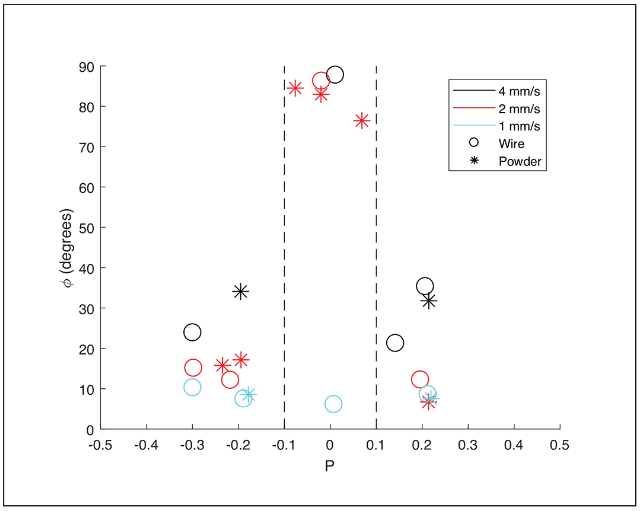

Fig. 7 — Tracer deformation φ as a function of position (P) across the wall thickness of the sample.

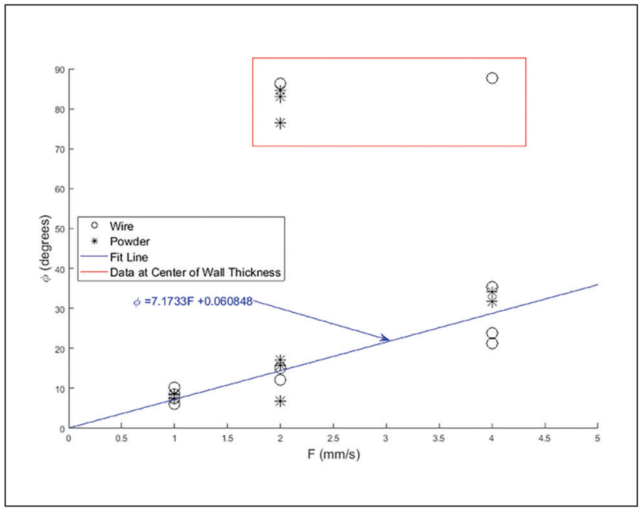

Fig. 8 — φ as a function of feed rate.

flow where the material near P = 0 flows in a primarily azimuthal direction and all other material flows in a primarily radial direction, as indicated by Fig. 7. The material outside the middle of the wall thickness undergoes a flow direction transition through a path with a radius that is independent of position, as indicated by the statistical study.

A cross-section of the proposed material flow model in the RZ plane is shown in Fig. 10. Path 1 captures the material flow indicated by tracers at $-0.1 < P < 0.1$ ($\varphi > 75$ deg). Path 2 captures the material flow indicated by tracers at $P < -0.1$ and $P > 0.1$ ($\varphi < 38$ deg).

The description of the material flow in each zone is defined as:

■ Material Flow Path 1

■ *Bifurcation Zone* — The microstructure in this zone can experience thermal recrystallization. The width of this zone is approximately 0.5 mm ($-0.1 < P < 0.1$). The flow is axial and there is no deformation in this zone.

■ *Heat Generation Zone (HGZ)* — Dynamic recrystallization occurs, allowing the material to undergo large values of strain and strain rate. The flow is primarily azimuthal.

■ Material Flow Path 2

■ *Un-deformed HAZ* — The characteristics of this zone are similar to the Bifurcation Zone, with the only distinction being the destination of material flow. The flow is axial and there is no deformation in this zone.

■ *Primary Shear Zone (PSZ)* — Thermo-mechanically driven recrystallization occurs. In this band, the material transitions from axial to primarily radial flow. The strain and strain rate in this zone are lower than those in Path 1.

■ *Post Deformation Zone* — Like the Un-deformed HAZ, there is material flow but no deformation. Thermal recrystallization and grain growth occur. The material flow in this zone is primarily radial. The amount of azimuthal flow (φ) is linearly related to the feed rate, as shown in Fig. 8.

The two paths defined have different material flow characteristics. The bifurcation of material flow necessitates a separate analysis for each path. The following sections evaluate the strain and strain rates the material undergoes through each path.

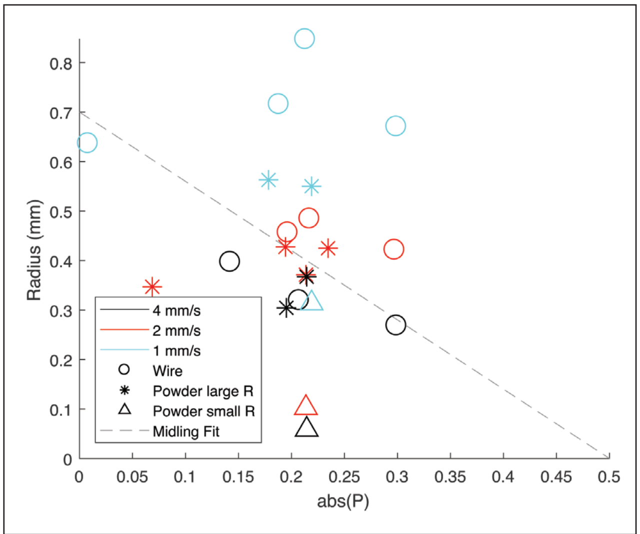

Fig. 9 — Radii (R) of tracers throughout wall thickness (P).

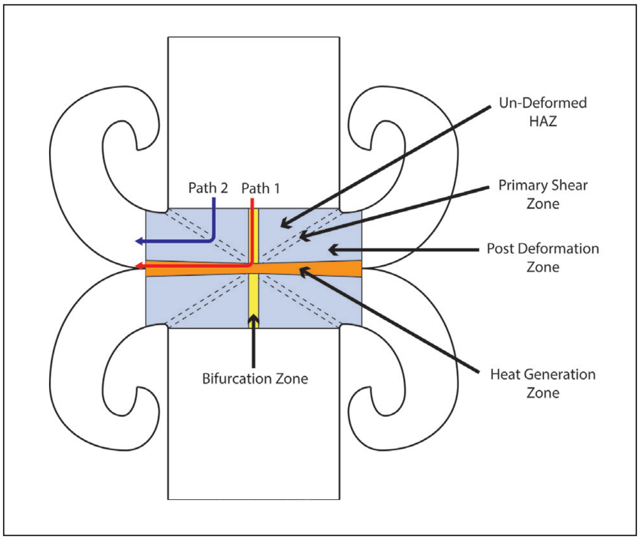

Fig. 10 — FW Material Flow Model.

Material Flow Path 1 Analysis

Path 1 consists of the un-deformed material flow in the Bifurcation Zone and the large azimuthal flow of the HGZ. Material flow in the HGZ is modeled using a previous study of the weld interface (Ref. 7). This model does not have a gradient of the azimuthal flow and strain rate, unlike the fully plasticized region in the model by Midling (Ref. 5).

The difference between the HGZ in the present model and previous studies of the weld interface is how the material enters the zone. Through analysis of the tracer data, the material outside the center of the wall thickness ($P < -0.1$ and $P > 0.1$) never comes into the HGZ. All material in the HGZ flows from the Bifurcation Zone.

The HGZ is named for the fact that most of the thermal energy needed to increase the material to sufficient temperatures for welding comes from the deformation at the weld interface.

Given the large azimuthal velocity and small thickness, the strain rate in the HGZ is expected to be large. The equation for the strain rate in the HGZ is (Ref. 7):

$$\dot{\gamma}_{HGZ} = \omega(ID + OD)/(16 * B) \quad (4)$$

where ω is the rotational velocity and B is the HGZ thickness.

The HGZ thickness was measured using tracer studies and metallography. The HGZ thickness is 0.15 mm as measured in welds with a powder tracer placed at the center of the wall thickness. The metallography indicated an HGZ thickness of 0.2 mm. With the HGZ thickness between 0.15 and 0.2 mm, the range in the strain rate calculated using Equation 12 is between 103.5 and 103.7.

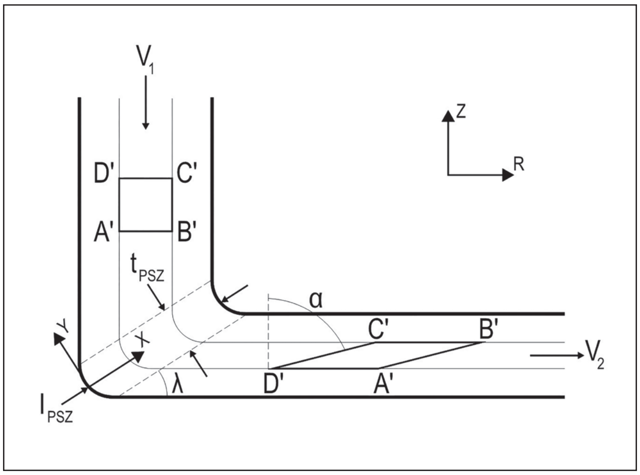

Fig. 11 — Model of the PSZ in the RZ plane.

Material Flow Path 2 Analysis

Path 2 captures the material flow of the tracers at $P < -0.1$ and $P > 0.1$. More than 80% of the material in the wall's thickness flows through Path 2. Since the velocity field proposed by Midling et al. (Ref. 7) does not agree with the current results for this path, a new model must be defined. For the model of the material flow in Path 2, this paper utilizes models of other processes that exhibit similar deformation. The processes that are used in the comparison are orthogonal machining (OM) and equal channel angular pressing (ECAP). The equations for strains and strain rates are non-linear and have been investigated in both ECAP (Ref. 8) and orthogonal machining by previous studies (Ref. 9).

This paper uses a thick shear zone analysis of orthogonal machining defined by Kishawy (Ref. 9) to model the material flow within the PSZ. The model was chosen for its ability to model the strain and strain rate within the PSZ. The deformation of a unit volume as it passes through the shear zone is depicted in Fig. 11 (adapted from [Refs. 9, 10]).

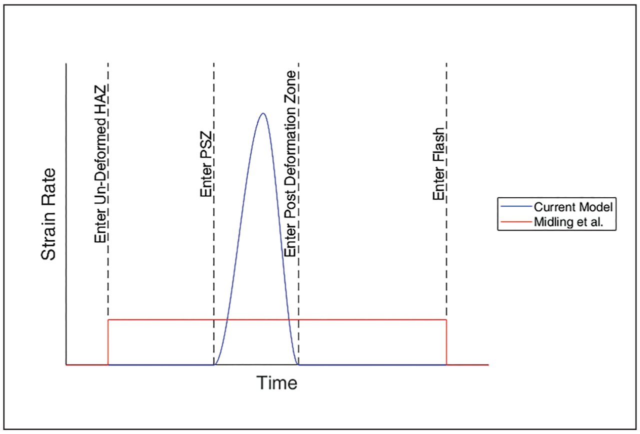

Fig. 12 — Strain rate through Path 2.

The angle α is not equal to the complement of λ (Ref. 11). α is not measured in the current investigation given that all strains have been found as a function of λ. The PSZ thickness (t_{PSZ}) and length (l_{PSZ}) are also shown in Fig. 11 and are necessary to calculate the strain rate.

The shear strain in the RZ plane depicted in Fig. 11 is given in both orthogonal machining ([Ref. 12] and ECAP [Ref. 8]) to be:

$$\gamma_X Y = \tan(\lambda) + \cot(\lambda) \quad (5)$$

The coordinate frame XYθ is used in this paper to facilitate a comparison of the strain reported in this paper and orthogonal machining.

There is one other shear strain induced upon a unit volume as it passes through the PSZ, which is due to the azimuthal flow. The azimuthal strain cannot be depicted in Fig. 11. In the RZθ coordinate system, the azimuthal shear is defined as:

$$\gamma_R \theta = \tan(\Phi) \quad (6)$$

The azimuthal shear rotated into the XYθ coordinate frame using a rotation matrix defined by Kelly (Ref. 13) is expressed as:

$$\gamma_X \theta = \tan(\Phi) * \cos(\lambda) \quad (7)$$

$$\gamma_Y \theta = -\tan(\Phi) * \cos(\lambda + 90°) \quad (8)$$

Previous studies in RFW have not analyzed individual components of strain, but have instead reported an equivalent strain. The individual true strains (Equation 9) are combined into an equivalent true strain using Equation 8 (Ref. 11):

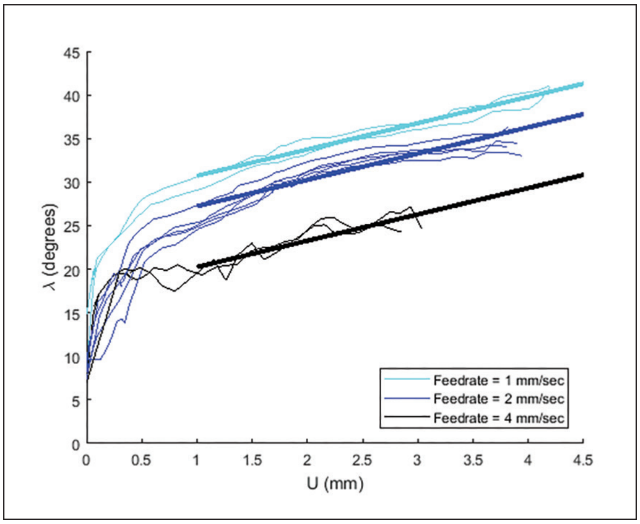

Fig. 13 — λ as a function of upset (U) for all welds.

$$\varepsilon_{eq} = \sqrt{(2(\varepsilon_X^2 + \varepsilon_Y^2 + \varepsilon_\theta^2) + (\gamma_{XY}^2 + \gamma_{X\theta}^2 + \gamma_{Y\theta}^2)/3} \quad (9)$$

The only strains present in the current model are the three shear strains. The strain rates can also be combined in a similar equation (Ref. 5).

Figure 12 shows the strain rate the material experiences throughout Path 2 in both the present model (blue line) and the model proposed by Midling et al. (red line). The bell curve of strain rate was defined in previous studies in orthogonal machining (Ref. 14). The mean strain rate within the PSZ in the current model is higher than that proposed by Midling et al. This is to be expected given that the transition from axial to radial flow in the model proposed by Midling et al. (Ref. 5) is continuous, while the transition observed in the marker data and model of the current study is more abrupt in the PSZ.

The mean value for the strain rate within the PSZ is defined to be half of the peak of the bell curve and is calculated as (Ref. 9):

$$\gamma_X Y Mean = F/(tPSZ * \cos(90° - \lambda)) \quad (10)$$

where F is feed rate and t_{PSZ} is PSZ thickness. Previous studies have not defined equations for $\dot{\gamma}_{X\theta}$ or $\dot{\gamma}_{Y\theta}$ since these strain rates are not present in either ECAP or orthogonal machining.

To calculate the values of $\dot{\gamma}_{X\theta\ Mean}$ and $\dot{\gamma}_{Y\theta\ Mean}$, the results of $\dot{\gamma}_{XY\ Mean}$ (Equation 7) are scaled by the ratio of the respective strains (Equations 4 and 5) and γ_{XY} (Equation 3). The strain rates can be calculated in this manner since it is assumed that the strain rate profiles for $\dot{\gamma}_{X\theta}$ and $\dot{\gamma}_{Y\theta}$ are all similar bell curves to $\dot{\gamma}_{XY}$.

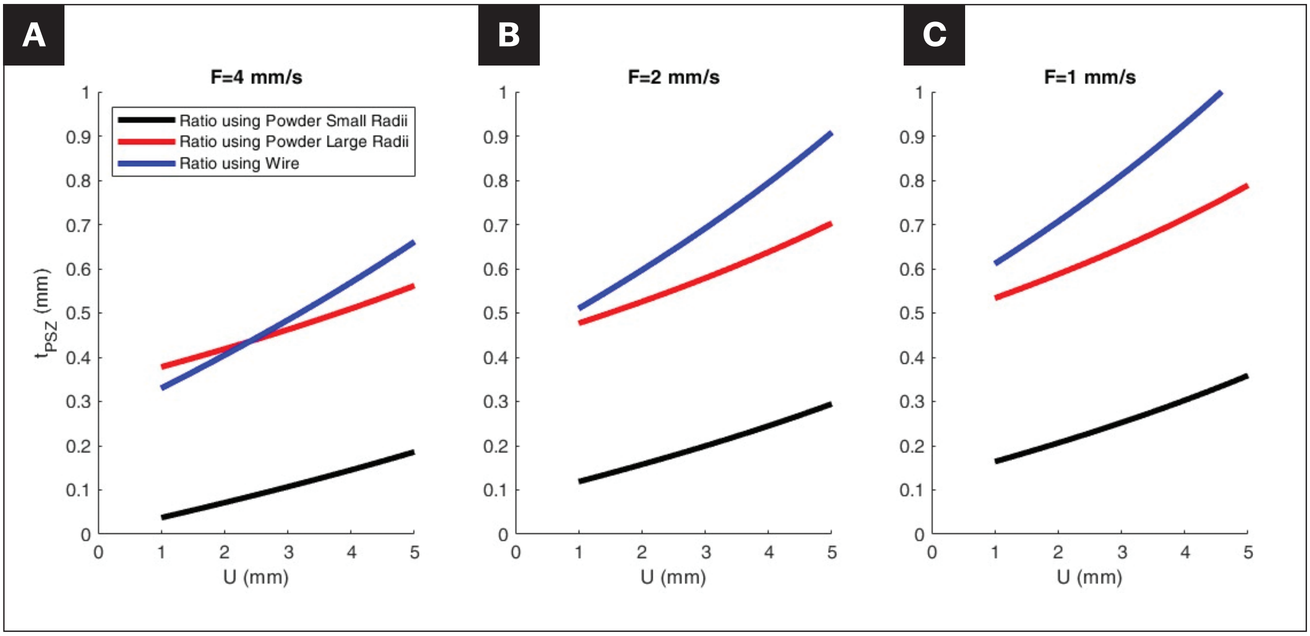

Fig. 14 — PSZ Thickness (t_{PSZ}) throughout the weld process as a function of weld upset (U) for all feed rates: A — 4 mm/s; B — 2 mm/s; C — 1 mm/s.

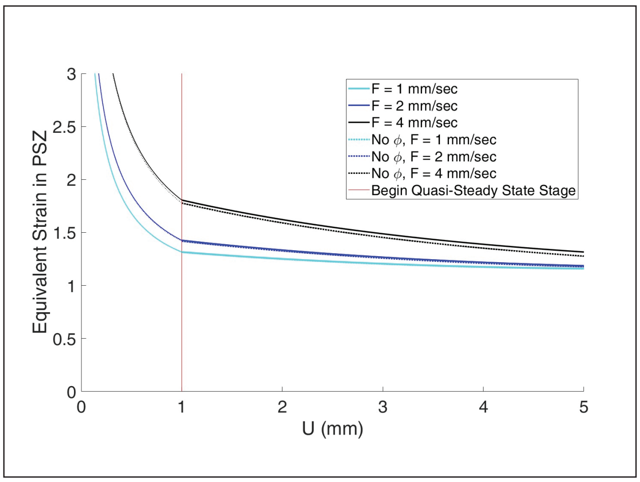

Fig. 15 — Equivalent strain as a function of upset (U) throughout the weld process.

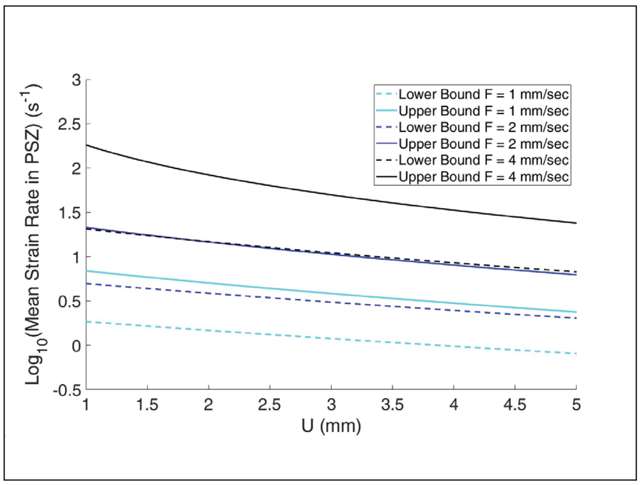

Fig. 16 — Mean equivalent strain rate as a function of upset (U) throughout the weld process.

The strains and strain rates discussed in this section are based on theoretical models, with no weld data used in the derivations of the equations. To calculate the strains and strain rates for the welds performed in this study, weld data is used.

Estimation of Variables Needed for Calculation of Strain and Strain Rate In the PSZ

The variables needed to calculate the strain and strain rate in Equations 5, 6, 7, and 9 are: F, φ, λ, and t_{PSZ}. These variables are estimated for each increment of upset so that strain and strain rate can be plotted as a continuous function throughout the weld process. The methods to calculate these variables are described below.

Measurement of F

The feed rate (F) is an input for the weld process and is constant throughout the quasi-steady state stage of the weld.

Estimation of φ

The azimuthal flow (φ) is necessary when computing azimuthal strains and strain rates. Analysis of the tracers in Path 2 ($P < -0.1$ and $P > 0.1$ in Fig. 7) show that there is a linear relationship between azimuthal flow and feed rate (Fig. 8). As discussed with the method of measuring φ, the value of φ is assumed constant throughout the weld process.

Estimation of λ

All strains and strain rates are a function of the angle λ (Fig. 11). This angle determines where the material transitions from axial to radial velocity. The angle λ can be seen in the results of microstructure studies, as shown in Fig. 3.

At any given increment of upset k, λ can be calculated from the following equation:

$$\lambda_k = \tan^{-1}\left(t_{FT,k}/(0.25 * (OD - ID))\right) \tag{11}$$

where $t_{FT,k}$ is instantaneous flash thickness at the increment of upset k. Flash thickness at each increment of upset must be estimated in order to calculate λ throughout the weld process.

By measuring the flash thickness at several locations and correlating each measurement to an upset (U), a relationship between flash thickness and upset can be calculated. A linear relationship is fit to the data during the quasi-steady state stages of the welds (upset >1mm), as shown in Fig. 13. The equation for the fit of the data to calculate λ is given as:

$$\lambda = 3.0205 * U - 3.4917 * F + 31.195 \tag{12}$$

Estimation of t_{PSZ}

The thickness of the PSZ (t_{PSZ}) is necessary in the calculation of the strain rates. In the proposed model, it is assumed that t_{PSZ} is uniform for all X (along the length of the PSZ) at any given increment of upset, as shown in Fig. 11. A uniform PSZ width is proposed to account for the fact that position variable P in Fig. 9 had no statistically significant effect on the tracer radius.

The t_{PSZ} during the weld process is unknown, but necessary to calculate the strain rate throughout the weld process. To calculate t_{PSZ} during the process, previous studies in orthogonal assumed that the ratio between t_{PSZ} and l_{PSZ} to be constant (Ref. 14).

In the present study, this ratio is calculated at the end of the weld using the results of the μCT radii. The fit of this calculation is defined as:

$$t_{PSZ}/l_{PSZ} = \begin{cases} 0.016 * \lambda - 0.085 & Wire \\ 0.008 * \lambda + 0.121 & Powder\ Large\ Radius \\ 0.008 * \lambda - 0.134 & Powder\ Small\ Radius \end{cases} \tag{13}$$

Using the fit of the ratio t_{PSZ}/l_{PSZ} (Equation 11), λ (Fig. 13), and the t_{PSZ} measurements at the end of the weld: t_{PSZ} is estimated throughout the weld process upset (U) using Equation 15 and shown in Fig. 14 for the three feed rates investigated.

The crossing of the wire and powder large radii lines in F = 4 mm/s is due to the extrapolation of the ratio depicted in Equation 13.

With the independent variables (F, φ, λ, and t_{PSZ}) available as continuous functions throughout the weld process, the strain and strain rate can be calculated using Equations 5, 7, 8, and 10.

PSZ Strain and Strain Rate

Figures 15 and 16 show the evolution of the equivalent strain and mean equivalent strain, respectively, throughout the weld process. In Fig. 16, the upper bounds (solid lines) represent the wire tracer data and the lower bounds (dashed lines) represent the powder small radii data, as shown in Fig. 14.

The strain far from the weld interface during the initial stage of RFW is expected to be much greater than the strain in the PSZ during the quasi-steady state stage. The flash thickness, and therefore λ, is much smaller in the initial stage, as shown in Fig. 13. These values for λ can be used to estimate the strain during the initial stage, as is depicted in the thin lines in Fig. 15. The material deformation is not investigated for this study. Therefore, the strain depicted in Fig. 15 is an extrapolation using the present analysis and should not be taken as the exact values of strain during the initial stage of RFW.

The magnitude of strain in Fig. 15 is similar to the strain reported by studies of orthogonal machining (Ref. 9) and ECAP (Ref. 10).

Strain rates in the PSZ, shown in Fig. 16, are higher than those reported in previous RFW studies, as depicted in Fig. 12. Midling (Ref. 5) reports strain rates around 100, which is the lowest value for the mean equivalent strain rate reported in the present model (Fig. 16). The reason for the difference is shown in Fig. 12.

There is a wide range in mean strain rates (almost two orders of magnitude) shown in Fig. 16. The size of this range is due to the compounding effect feed rate has on decreasing both λ and PSZ thickness. Faster welds have larger values of strain and the distance over which the deformation occurs is smaller.

Figure 15 also shows the difference in strain when the azimuthal flow in Path 2 is assumed to be zero by comparing the dotted lines compared to solid lines. The dotted lines were calculated by removing $\gamma_{R\theta}$ and $\dot{\gamma}_{R\theta}$ in the calculation of equivalent strain and equivalent strain rate, respectively (Equation 9). The assumption of no azimuthal flow results in an error of 3% in the equivalent true strain and < 1% in the mean equivalent true strain rate. The error in the strain rate is so small that it cannot be depicted in Fig. 16.

The application of this model to different materials and geometries does not require a significant amount of work. With the assumption of no azimuthal flow in Flow Path 2, the only independent variables needed in future studies are λ and t_{PSZ}. Therefore, future studies will only have to calculate a new fit similar to Figs. 13 and 14.

The values for strain and strain rate reported in the current paper are not to be used as absolute bounds of RFW of thin-walled tubes but instead, be viewed as ranges for typical values in normal operating parameters. Higher or lower strain rates could be accomplished with faster or slower feed rates than those used in the current experiment.

Conclusions

The present study provides new 3D insights into the material flow of RFW using tungsten tracers. A new material flow model has been proposed that incorporates the insights found in the tracer study. Similar to the model proposed by Midling (Ref. 5), the current model consists of two main regions of deformation regions. The main differences between the present model and previous models are: 1) the location and volume of material that interacts at the interface (Path 1), and 2) the mode of deformation in Path 2 (Fig. 10). Based on the results and analysis present herein, the following conclusion can be made:

1. The material located close to the centerline of the sample wall is the only material that interacts with the weld interface (Path 1, Fig. 10). Material flow in Path 1 is primarily azimuthal and exhibits strain rates between $10^{3.5}$ and $10^{3.7}$. The strain in this region is sufficient to sustain continuous dynamic recrystallization. The combined width (both sides of the bond line) of this zone is between 0.15 and 0.2 mm over the range of parameters investigated.
2. Approximately 800% of the wall thickness flows through Path 2. Material flow in this path is primarily radial flow. Unlike previous studies, the present work indicates that deformation in Path 2 occurs abruptly, occurring within a narrow band, e.g., the Primary Shear Zone (PSZ). The angle of the PSZ is primarily dependent on the federate: decreases with increasing force or federate.
3. The deformation in the PSZ is similar to that observed in both orthogonal machining and equal channel angle pressing. Using formulation from these, the strain and strain rates in the PSZ are much lower than those in Path 1. Strain and strain rates in this region range from 1.2 and 1.75 and 10^{0} and $10^{1.7}$ s^{-1}, respectively.
4. Given the significant differences in strain and strain rates between the HGZ and PSZ, most of the heat generated in RFW is generated from a small volume of material in Path 1.

Acknowledgments

A special thanks to Martin Morra and Nicole Kucza at GE Global Research for the micro CT analysis and technical discussion. Funding and financial support for this work was provided by Brigham Young University.

References

1. Maalekian, M. 2007. Friction welding – critical assessment of literature. *Science and Technology of Welding and Joining* 12(8): 738–759. DOI: 10.1179/174329307X249333

2.Grant, B., et al. 2009. Finite element process modelling of inertia friction welding advanced nickel-based superalloy. *Materials Science and Engineering: A* 513–514: 366–375. DOI: 10.1016/j.msea.2009.02.005

3. Zhang, Q. Z., Zhang, L. W., Liu, W. W., Zhang, X. G., Zhu, W. H., and Qu, S. 2006. 3D rigid viscoplastic FE modelling of continuous drive friction welding process. *Science and Technology of Welding and Joining* 11(6): 737–743. DOI: 10.1179/174329306X153222

4. Li, P., Li, J., Li, X., Xiong, J., Zhang, F., and Lian, L. 2015. A study of the mechanisms involved in initial friction process of continuous drive friction welding. *Journal of Adhesion Science and Technology* 29(12): 1246–1257. DOI: 10.1080/01694243.2015.1022499

5. Midling, O.T., and Grong, O. 1994. A process model for friction welding of Al-Mg-Si alloys and Al-SiC metal matrix composites—I. Haz temperature and strain rate distribution. *Acta Metallurgica et Materialia* 42(5): 1595–1609. DOI: 10.1016/0956-7151(94)90369-7

6. Kessler, M., Suenger, S., Haubold, M., and Zeah, M. F. 2016. Modeling of upset and torsional moment during inertia friction welding. *Journal of Materials Processing Technology* 227: 34–40. DOI: 10.1016/j.jmatprotec.2015.07.024

7. Francis, A., and Craine, R. E. 1985. On a model for frictioning stage in friction welding of thin tubes. *International Journal of Heat and Mass Transfer* 28(9): 1747–1755. DOI: 10.1016/0017-9310(85)90148-6

8. Lee, D. N. 2000. An upper-bound solution of channel angular deformation. *Scripta Materialia* 43(2): 115–118. DOI: 10.1016/S1359-6462(00)00377-8

9. Kishawy, H. A., and Pang, L. 2012. A phenomenological modeling of deformation during metal cutting: A modified thick shear zone analysis. *Proceedings of the Institution of Mechanical Engineers, Part B: Journal of Engineering Manufacture* 226(9): 1431–1441. DOI: 10.1177/0954405412450380

10.Valiev, R.Z., and Langdon, T.G. 2006. Principles of equal-channel angular pressing as a processing tool for grain refinement. *Progress in Materials Science* 51(7): 881–981. DOI: 10.1016/j.pmatsci.2006.02.003

11. Iwahashi, Y., Wang, J., Horita, Z., Nemoto, M., and Langdon, T. 1996. Principle of equal-channel angular pressing for the processing of ultra-fine grained materials. *Scripta Materialia* 35(2): 143–146. DOI: 10.1016/1359-6462(96)00107-8

12. Lalwani, D.I., Mehta, N.K., and Jain, P.K. 2009. Extension of oxley's predictive machining theory for johnson and cook flow stress model. *Journal of Materials Processing Technology* 209(12): 5305–5312. DOI: 10.1016/j.jmatprotec.2009.03.020

13.Kelly, P. 2013. *Solid mechanics part I: An introduction to solid mechanics*. A Creative Commons Attributions.

14. Oxley, P. 1989. *The mechanics of machining: An analytical approach to assessing machinability*. Ellis Horwood Limited.

CALEB BROWN is with Northrop Grumman, Salt Lake City, Utah. **TRACY W. NELSON** (*nelsontw@byu.edu*) is with BYU Manufacturing Engineering, 265 CTB, Provo, Utah. Lastly, **CARL SORENSON** is with Mechanical Engineering, Provo, Utah.